CHAPTER 3

Defect induced ferromagnetic ordering and room temperature negative magnetoresistance in MoTeP

3.1 Introduction

The realization of the Weyl semimetals (WSMs) has sparked extreme research interests in condensed-matter physics community since it provides the recognition of the Weyl fermions. This topological semimetal is associated with the lack of time-reversal or inversion symmetry. The concept of WSMs can be categorized into two ways. In type-I WSMs, the linear nondegenerate band crossings lead to a point like Fermi surface (FS) when the chemical potential is adjusted to the energy of Weyl Points (WPs). The hole and electron pockets form the WPs [112], [113] in the type-II WSMs unlike the case of type-I in which band crossings produce the WPs. A finite density of states at the chemical potential is created due to overlapping of these electron and hole pockets over a range of energies[49], [114], [115]. Again, the type-I WSM obeys Lorentz invariance, in contrast, type-II does not. These Weyl points are two-fold degenerate and always come in pairs with opposite chirality, namely, a source and a sink of the Berry curvature [116], [117]. The concept of type-II WSMs was brought forward by studying the topological properties of $MoTe_2$, WTe_2 and their alloy $Mo_{1-x}W_xTe_2$ [56], [118], [119]. With time many researches were devoted to 2D transition metal dichalcogenides materials (TMDs) with chemical formula MX_2, where M is a transition metal and X is a chalcogen atom (S, Se or Te) due to their significant electronic and optoelectronic properties. Very recently, 3D TMDs WP_2 and MoP_2 were predicted to host four pairs of type-II Weyl points below the Fermi energy with a unique feature of having same chirality for the nearest WPs[120].

In addition, WSMs are in general renowned for their negative longitudinal magnetoresistance (NLMR) induced by chiral anomaly[121], [122], which refers to the non-conservation of chiral charge around the Weyl nodes when applied electric and magnetic fields are non-orthogonal ($E.B \neq 0$). The experimental measurement of NLMR is very sensitive, and especially for type-II WSMs, the NLMR can only be observed along

specific crystalline directions and in samples with appropriate chemical potential[123], [124]. In type-I Weyl semimetals, the chiral anomaly always appears regardless of the direction of the applied magnetic fields.

To best of our knowledge, so far, the NLMR has not been reported for $MoTe_2$[125]. Furthermore, there are many reports on the spin-orbit coupling and the interesting consequences of electrical and optical properties in these systems. However, there are very limited, and mostly theoretical studies on intrinsic magnetism based on monolayer structure calculation[126]–[129]. Theoretical and experimental work shows that in the absence of crystalline imperfections, the Mo-based TMDs are nonmagnetic[130]–[132]. Therefore, by adding defects one may induce magnetism into these materials and this ability can open up a host of new opportunities for spintronic applications. Our study indicates that it is a near perfect compensated semimetal containing defect induced ferromagnetism.

3.2 Methods

3.2.1 Structural characterization We have performed Le-Bail refinement of the powder XRD data (CuK_α radiation) of MoTeP single crystal to obtain the lattice parameters. The extracted lattice parameters are a= 3.3759(52) Å, b= 6.2907(93) Å and c= 13.8629(28) Å whereas the calculated α, β and γ values are 90˚, 94.82˚ and 90˚. The obtained lattice parameters are consistent with 1T′ ($P2_1/m$) family of compounds[133].

3.2.2 Material characterization Magneto-transport properties measurements were performed in a Quantum Design Physical Properties Measurement System (PPMS) using a five-probe configuration at Institute for Solid State Physics, University of Tokyo, Japan by using physical property measurement system (PPMS) with varying magnetic field up to 7 T. The measurements were performed in a standard Hall bar geometry i.e electrical current was applied along the b axis, and magnetic field perpendicular to the b axis.

Magnetic measurements (both temperature and magnetic field dependent) were performed using quantum design SQUID magnetic properties measurement system (MPMS). Temperature dependent Raman study was executed by Horiba LabRam HR evolution spectrometer. The sample was irradiated with 633 nm He-Ne laser. The sample was cooled from 300 to 190 K by liquid nitrogen when taking Raman measurements at different temperatures.

3.2.3 Density functional theory (DFT) calculations We performed DFT calculations using ABINIT package[134] with a projector-augmented-wave (PAW) method. We adopted generalized gradient approximation (GGA) as exchange-correlation proposed by Perdew-Burke-Ernzerhof (PBE). All atoms of MoTeP were fully relaxed with conjugate-gradient algorithm until a force is less than 0.01eV $Å^{-1}$ and the energy convergence criteria was put to 10^{-6} eV. The electronic calculations were performed using Γ-centred K-mesh of 15×9×5 with a plane-wave energy cutoff of 19.1096 Ha (520 eV), spin orbit coupling (SOC) was included in the calculations. We used optimized lattice parameters (a = 3.3418(56) Å, b = 6.0887(71)Å and c= 13.3433(95)Å for the theoretical calculation of MoTeP. For the spin-polarised DOS calculations vacancy and antisite defects were created inside the crystal structure. Additionally, we checked GGA+U with U=0.0367493 Ha (1 eV), however inclusion of Coulomb interaction U does not affect our results. The output files (.agr) were analysed in XMGRACE[135] software.

3.3 Results and discussion

3.3.1 Zero field resistivity behavior The temperature evolution of the resistivity ρ_{xx} shows metallic character throughout the measured temperature range as shown in Figure 3.1(a). The longitudinal resistivity ρ_{xx} indicating dominant electron-electron and electron-phonon scattering at low temperature as depicted in figure 3.1(a) inset. MoTeP shows resistivity

36.55 μΩ-cm at 2K and this reaches to 963.47 μΩ-cm at 300 K. Thus the residual resistivity ratios (RRRs) = ρ(300 K)/ρ(2K)=26.41 suggesting good crystalline quality of the sample. This value of RRR is consistent with several topological semimetals[136]–[138].

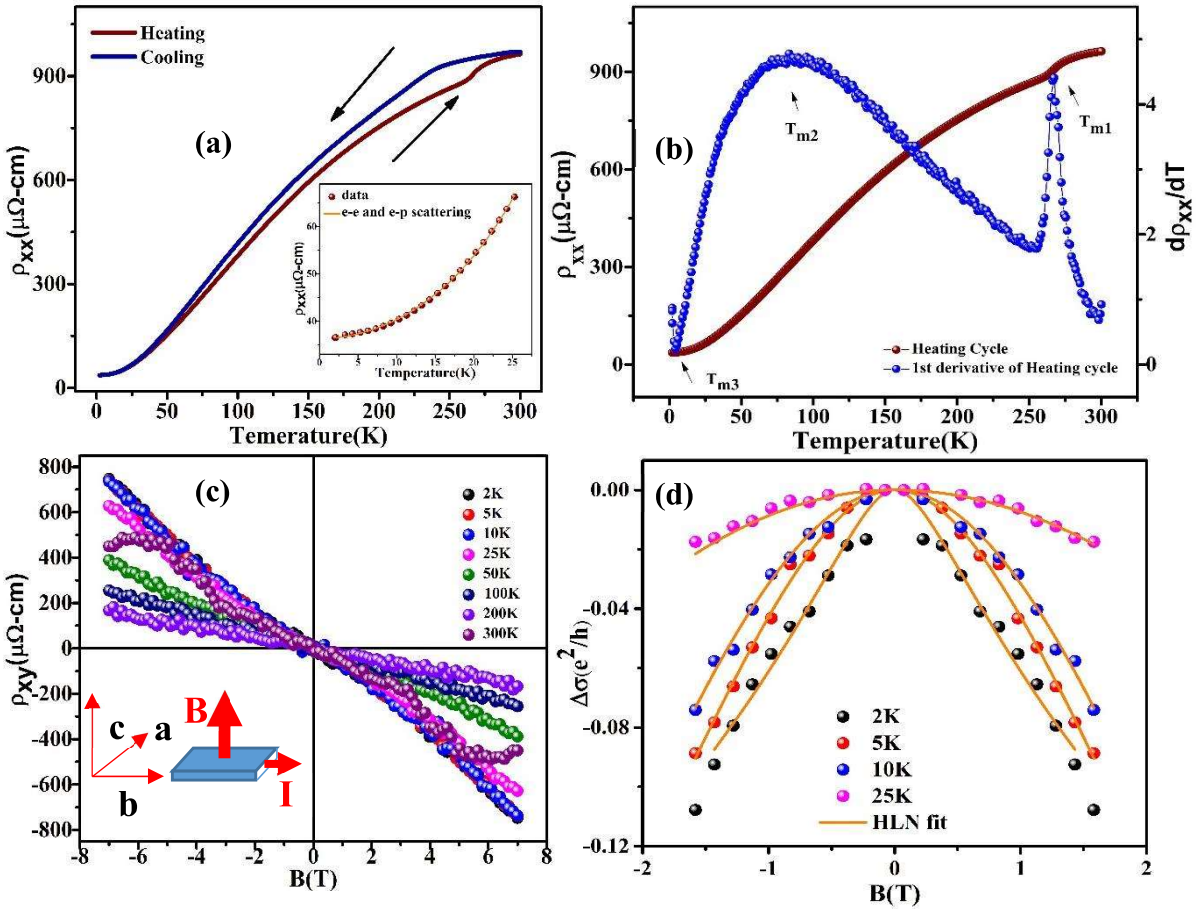

Figure 3.1 (a) Thermal hysteresis of temperature dependent resistivity of 1T′ MoTeP, **inset:** low temperature resistivity data, orange solid line is a fit of electron-electron and electron-phonon scattering terms $\rho(T) = \rho_0 + aT^2 + bT^5$, **(b)** temperature evolution of ρxx and $d\rho_{xx}/dT$ at zero magnetic field, **(c)** Field dependence of Hall data ρ_{xy} at various temperatures, **inset:** measurement geometry, **(d)** low- field low-temperature conductivity data, solid orange line shows HLN fitting to $\Delta\sigma(e^2/h)$ at various temperatures.

The temperature dependence of the resistivity at low temperature can be accounted for by the usual combination of Fermi liquid and electron-phonon scattering mechanisms by fitting to $\rho_{xx}(T) = \rho_0 + aT^2 + bT^5$, where ρ_0 = ρ(T = 0 K) with a and b being fitted

parameters (figure 1a inset). Three temperature regions T_{m1}, T_{m2}, T_{m3} are marked with arrows in figure 3.1b. The observed hysteresis around T_{m1}~250 K between the warm-up and the cool-down curves (figure 3.1a) is ascribed to the structural phase transition from the 1T′ to the T_d structure which is consistent with $MoTe_2$[139], [140]. This structural phase transition is confirmed by temperature dependent Raman spectroscopy (supplementary). The coexistence of 1T′ and T_d phase is the possible reason behind the hysteresis over a long range of temperature. This type of hysteresis behavior is common in $MoTe_2$[139]. The $d\rho_{xx}(T)/dT$ curve exhibited a broad peak around the temperature ~75K (marked as T_{m2}), which suggests the possible change in the electronic structure of T_d-MoTeP. This is also consistent with the reports on $MoTe_2$[60], [141]–[144]. However, the temperature (T_{m2}) for $MoTe_2$ is ~50K. Temperature dependent mass anisotropy was also reported around T_{m2} in $MoTe_2$ by Chen et al [142]. We identified the temperature as T_{m3} where 1st derivative of ρ_{xx} becomes minimum which is also known as the turn on temperature[142]. Therefore, the observed transport behavior in MoTeP is consistent with the Weyl semimetal $MoTe_2$[139]. In T_{d-} phase inversion symmetry is broken which is the necessary condition for a material to have Weyl semimetal phase[55], [56], [58] In the present investigation, the existence of T_d-phase in MoTeP is a possibility of this material to be Weyl semimetallic. Furthermore, turn on behavior is commonly attributed to field induced metal insulator transition and is well familiar among extremely large MR (XMR)[60], [139], [145]–[147]. Importantly, Q. L. Pei and his group[60] suggested the electronic structure change (near 50K) as the necessary condition for the presence of the turn-on phenomenon in WTe_2 and T_d-$MoTe_2$.

3.3.2 Hall Effect study Figure 3.1(c) displays the magnetic field dependence of Hall resistivity ρ_{xy}. From the Hall resistivity behaviour it is clear that the conduction carriers are dominated by electrons which is consistent to that of other Weyl semimetals[148], [149]. However, the $\rho_{xy}(B)$ shows non-linear behavior and with increase of temperature the

deviation from linearity of $\rho_{xy}(B)$ increases and finally at 300K it shows unusual non-linearity (S-shaped) at high field. This nonlinear $\rho_{xy}(B)$ implies the existence of both electrons and holes. The S-shaped nonlinearity is similar to that of topological single crystal system $Bi_{1-x}Sb_x$[150]. In order to determine carrier mobility and carrier density for both type of charge carriers we executed two-carrier model fit with our σ_{xy} and σ_{xx} data, where the field dependence of the conductivity tensor is given by

$$\boldsymbol{\sigma_{xy} = [n_e \mu_e^2 \frac{1}{1+(\mu_e B)^2} - n_h \mu_h^2 \frac{1}{1+(\mu_h B)^2}]eB} \quad \textbf{(3.1)}$$

where Hall conductivity $\boldsymbol{\sigma_{xy} = -\frac{\rho_{xy}}{\rho_{xx}^2+\rho_{xy}^2}}$ **(3.2)**

Here, $n_e(n_h)$ and $\mu_e(\mu_h)$ are electrons (holes) carrier densities and mobilities, respectively and σ_{xy} is the Hall conductivity. Figure 3.2(a) illustrates the temperature dependence of the Hall conductivity and their respective two-band model fit. The fitting of eq. 1 yields electron and hole densities 0.188×10^{19} and 0.182×10^{19} cm^{-3} respectively at 2K. The electron and hole mobilities are 2.216×10^4 and 2.196×10^4 $cm^2/V.s$. The extracted parameters n_e, n_h, μ_e, μ_h and their temperature evolution along with a comparative result of n_h/n_e and μ_h/μ_e is also shown in figures 3.2(c) and 3.2(d). These values show that the magnetotransport properties in MoTeP is primarily influenced by electron type charge carriers and a near perfect electron-hole compensation scenario is present in this system at low temperature. These values are comparable to many Dirac Cd_3As_2, $ZrTe_5$[151], [152] and other semimetallic $MoTe_2$, WTe_2, LaSbTe, VAl_3 [141], [153]–[155] systems. However, our hole mobility is two order less than WP_2 [147]. The carrier density is almost constant from 2 to 15K. However, the mobility of both type of carriers decreases with increase in temperature. Above 50K hole mobility and electron density increases rapidly and there is a change in the temperature dependence of the electron and hole density and/or mobility.

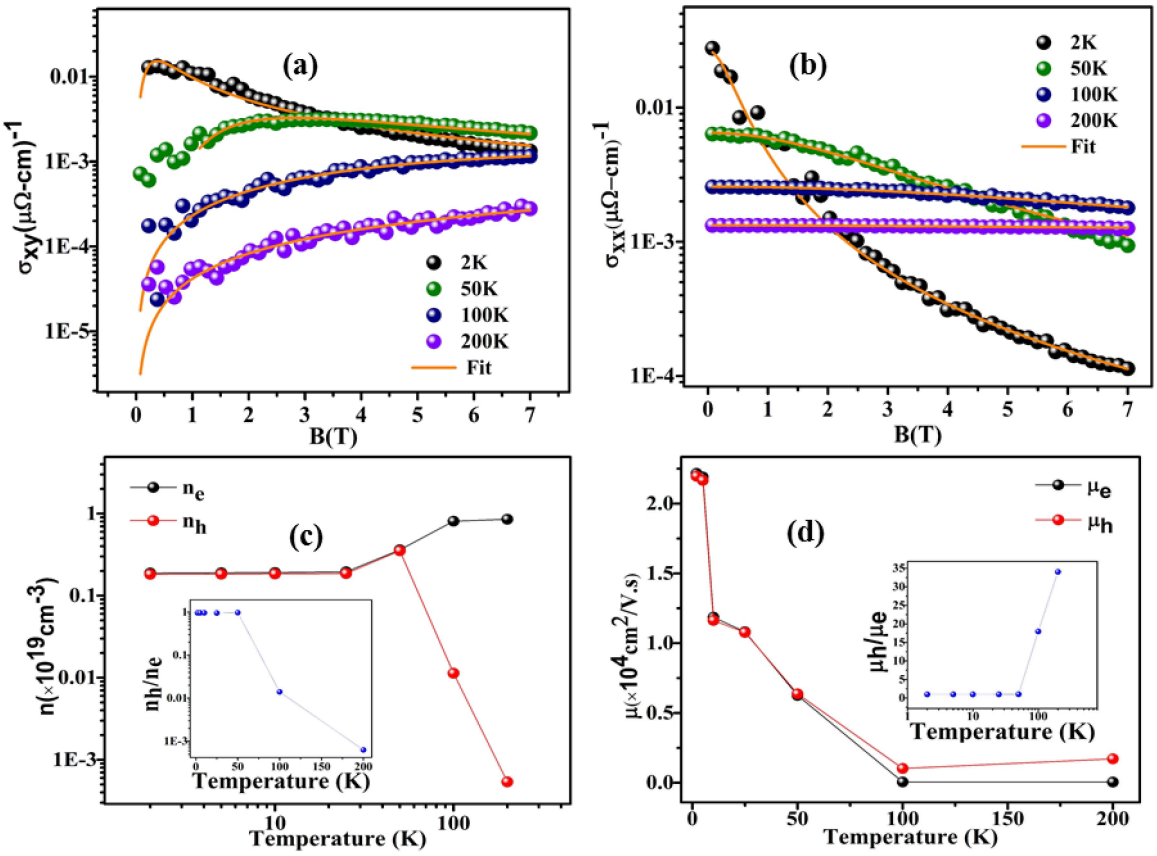

Figure 3.2 (a), (b) Field dependence of Hall conduvtivity σ_{xy} and longitudinal conductivity σ_{xx} at 2,50,100 and 200K, orange solid lines are their respective two-carrier model fit with equations 1 and 3, **(c)** density of electrons n_e (black circle) and density of hole n_h(red circles) as a function of temperature extracted from σ_{xy}, **inset:** ratio of n_h and n_e as a function of temperature, **(d)** electron mobility μ_e (black circle) and hole mobility μ_h (red circles) and their ratio μ_h/μ_e, **inset:** as a function of temperature.

The electron and hole density extracted at room temperature $n_e \sim 0.177\times10^{19}$ cm^{-3}, $n_h \sim 0.173\times10^{19}$ cm^{-3} and their mobilities are $\mu_e \sim 0.196\times10^4$ $cm^2/V.s$ and $\mu_h \sim 0.198\times10^4$ $cm^2/V.s$ respectively. Furthermore, it is observed that the amplitude of the nonlinear S-shaped becomes flat with increasing n_e. Also, hole plays dominant contribution at this temperature with an increase in μ_h. In order to assess the accuracy of the parameters obtained for charge density and mobility we further fitted our σ_{xx} (eq. 3) data using

$$\sigma_{xx}=\left[\frac{n_e\, e\, \mu_e}{1+(\mu_e B)^2}+\frac{n_h\, e\mu_h}{1+(\mu_h B)^2}\right] \qquad \textbf{(3.3)}$$

where longitudinal conductivity $\sigma_{xx} = \frac{\rho_{xx}}{\rho_{xx}^2+\rho_{xy}^2}$ **(3.4)**

σ_{xx} is longitudinal resistivity (Figure 3.2b) in transverse magnetic field and current configuration. The obtained electron density n_e~0.188×10^{19} and hole density n_h~ 0.182×10^{19} cm^{-3} and the extracted electron mobility μ_e~2.218×10^4 $cm^2/V.s$ and hole mobility μ_h~2.164×10^4 $cm^2/V.s$ at 2K. The hole density increases beyond 50K whereas and electron-hole density becomes comparable at low temperature. As evident from the figure 2c n_e increases with temperature whereas n_h decreases above 50K. This is similar to $MoTe_2$[142]. In addition, mobility of both type of carriers decreases with increasing temperature. The ratio n_h/n_e decrease above 50K. Above a certain temperature hole mobility becomes larger than electron mobility. Finally, at room temperature both the carriers are taking part in the transport. This might be the reason of S-shaped nature of Hall data at 300K.

It is worthwhile to mention that the large carrier mobility is decisive to the XMR effect in Weyl semimetal [141]. In the present case, in T_d-MoTeP we also observe (discussed above) the large carrier mobility. However, such colossal XMR effect is absent in the present system due to dominating ferromagnetic ordering effect (discussed below). The decreased mobility at high temperature can be expected as electron-phonon scattering is dramatically increased at high temperature.

3.3.3 Magnetization behavior In order to find out the magnetic ordering we have also measured the magnetization behavior in MoTeP. Interestingly, we have found the presence of magnetic hysteresis in M(B) (figure 3.3d) indicating the ferromagnetic ordering in this compound. The magnitude of the loop decreases with increasing temperature. The estimated coercive fields are 278 and 195 Oe at 5K and 300K, respectively. This type of long range ordering is also reported in the pioneering work by Z. Guguchia[156] for the

compound 2H-$MoTe_2$ and $MoSe_2$. Such ferromagnetism was induced by defects like metal vacancies and chalcogen-metal antisites disorder. The Mo vacancy can also induce spin polarization with large magnetic moments[131]. Presence of vacancy (V_{Mo}, V_{Te}, V_P) and antisite defects (Te_P, Mo_{Te} Te_{Mo}) has been considered as most common point-defects in the 2D materials like $MoTe_2$ [126].

We have demonstrated M-T behavior for the present investigation to probe the ferromagnetism into the sample. However, the data reveals a strong bifurcation between ZFC and FC cycle (Figure 3.8b) which might be due to ferromagnetic nature of the compound. This M-T behavior is in line with [156] defect produced $MoTe_2$. Long range magnetic ordering persists below the temperature T_1. The magnetic moment continuously increases below this point. Below temperature T_2, short range ordering (small ferromagnetic domains) is possibly present and responsible behind the inhomogeneous magnetism in the sample. This trend is similar to 2H-$MoTe_2$ and 2H-$MoSe_2$[156]. The bifurcation in the ZFC and FC response also suggests that different ferromagnetic domains tend to cancel out (anti-align) after ZFC. The domains will be aligned if we do field cooling. Again, the undulating magnetic domains of the MFM image (Figure 3.8c) is due to the ferromagnetic state, this is similar to the previous report on MoS_2[130].

3.3.4 Effect of magnetic field on longitudinal resistivity The longitudinal resistivity ρ_{xx} measured under perpendicular current and magnetic field configuration. This ρ_{xx} follows a nearly quadratic dependence on magnetic field indicating no sign of saturation. Magnetoresistance [MR= $\{\rho_{xx}(7T) - \rho_{xx}(0T)\}/\rho_{xx}(0\ T)$, ρ_{xx} is the longitudinal resistivity] reaches 77.831% at 2 K. This MR value is relatively small compared to the other reports

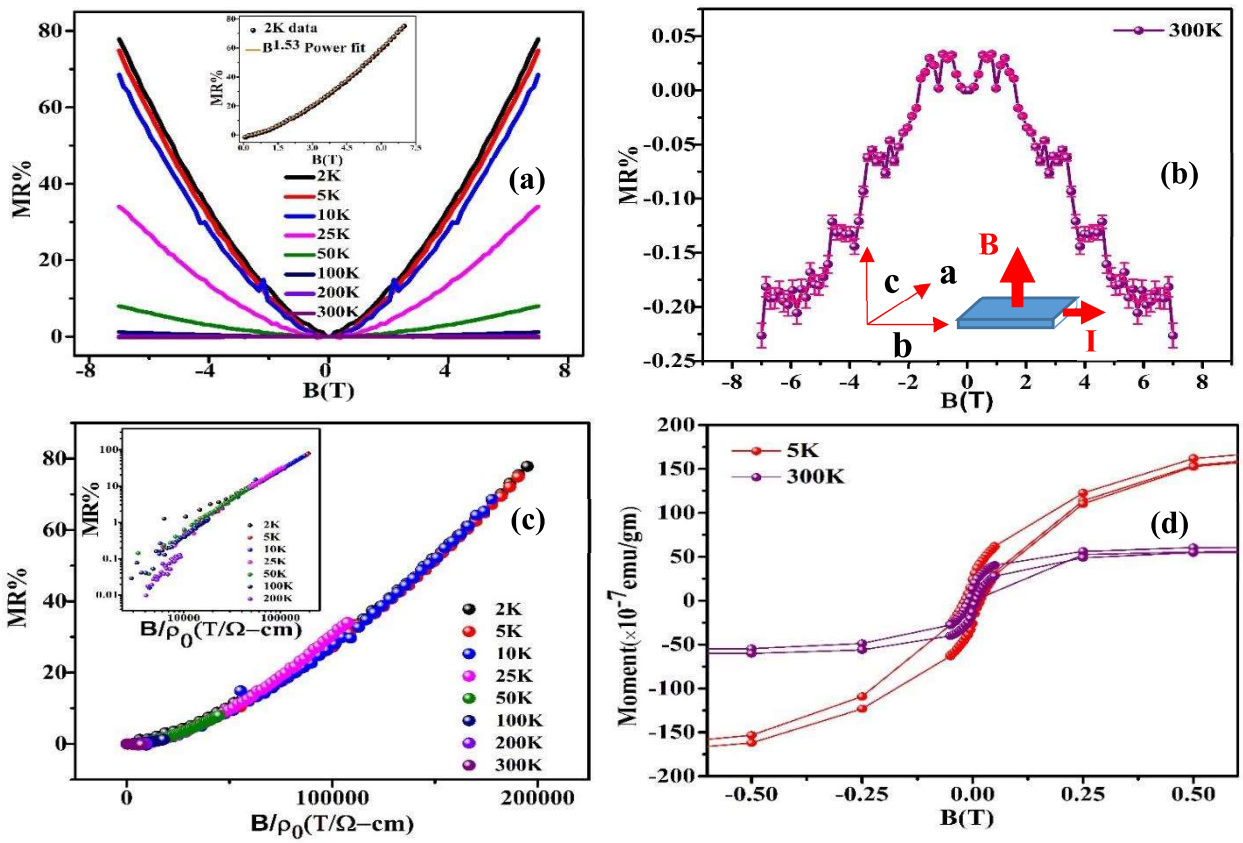

Figure 3.3 (a) Magnetic field dependent MR% at various temperatures ranging from 2K-300K, inset shows 2K MR% with a power law fit (orange solid line), **(b)** clear pictorial view of positive MR at low field and negative MR at high field for 300K data, **inset:** measurement geometry, **(c)** Kohler's scaling of MR% as a function of B/ρ_0 up to 300K, **inset:** Kohler plot on logarithmic scale up to 200K, **(d)** M-B magnetic hysteresis curve taken at 5K and 300K.

on XMR family of compounds like $MoTe_2$, WTe_2, MoP_2 and WP_2[142], [148], [149], [157]. Moreover, electron-hole compensation and electronic changes near 60K (50K) was considered as the driving force behind the XMR in $MoTe_2$ (WTe_2)[149], [158]. Particular orbital texture on the electron pocket was also proposed as a possible reason behind the XMR in $MoTe_2$[142]. The MR% value is gradually suppressed with increasing temperature. The MR% decreases to 0.113% at about 200K (figure 3.3a). A clear view of 300K MR% data with error bar is represented in figure 3.3(b). The positive MR weakened as the temperature is increased and finally the MR displayed mixed behavior from positive in low fields to negative in high fields when the temperature increased to 300K. However,

all the data in Figure 3.3c can be scaled onto a single line when MR plotted as a function of B/ρ_0. However, deviation from the single line is observed above 50K when plotted on log-log scale (inset of 3.3c). Departure from the scaling signify the existence of both type of charge carrier in the system supporting the Hall data. Multiband effect with different scattering time was also considered as a reason behind the breakdown of Kohler's rule in MoP_2[159]. The dominance of phonon scattering at high temperature might also be the reason of this deviation[160]. However, according to semi-classical two-band theory, the validity of Kohler's rule with MR $\propto (B/\rho_0)^2$ suggests an XMR or perfect electron-hole compensated system. Violation of Kohler's rule is common in XMR materials, such as LaBi, TaAs, $TaAs_2$, $NbAs_2$, $NbSb_2$, and LaSbTe [154], [161]–[164]. Our trial to fit the Kohler's law ($\boldsymbol{MR = c(\frac{B}{\rho_0})^m}$) yields c=25 $(\mu\Omega\text{-cm/T})^{1.65}$ and m=1.65. The value of m~1.65 is away from a perfect electron-hole compensation (m~2) situation. The deviation in Kohler's scaling is also in line with our nonlinear Hall data and multiband transport above 50K. We performed a power law (figure 3.3a inset) with MR% data at 2K and fitting yields n=1.53 which shows a subquadratic field dependence[165], [166]. $MR \sim B^n$ where n is predicted to be 2 for semimetals with perfect electron-hole compensation. Our fitted n~1.53 value also conveys the results of electron dominating transport at low temperature in accordance with the Hall data.

Nevertheless, the chiral anomaly induced negative LMR and positive transverse magnetoresistance (TMR) as a result of Lorentz force is fingerprint of the type-II Weyl semimetals[60], [147]. In our case MoTeP also shows positive MR up to 200K due to Lorentz force in perpendicular current and magnetic field configuration. The MR near B=0 is also positive at 300K. On the other hand, under the application of external magnetic field the decrease in resistivity with increasing temperature is systematic in T_d-MoTeP up to 200K, as expected in semimetallic systems. The 2K MR curve shows a small cusp-like

feature at low field suggesting the presence of the weak anti-localization (WAL) effect. The conductivity change $\Delta\sigma=\Delta\sigma(B)-\Delta\sigma(0)$ arising from the quantum interference effects is explained by the Hikami- Larkin-Nagaoka (HLN) theory[167]-

$$\Delta\boldsymbol{\sigma} = \boldsymbol{\sigma(B)} - \boldsymbol{\sigma(0)} = \boldsymbol{A}\left[\boldsymbol{\psi}\left(\frac{1}{2}+\frac{h}{8\pi eBL_{\varphi}^{2}}\right) - \boldsymbol{ln}\left(\frac{h}{8\pi eBL_{\varphi}^{2}}\right)\right] \quad \textbf{(3.5)}$$

where $\boldsymbol{A} = \frac{\alpha e^2}{\pi h}$ and α is a constant equal to 1 or -1/2 for weak localization or anti-localization respectively. ψ is digamma function, L_φ is the phase coherence length. We have calculated magnetoconductance per conduction channel $\Delta\sigma/Z^*$ (Z^* is no. of conduction layers). One 2D layer corresponds to e^2/h conductance and that is equal to 2 QL thickness i.e. 2nm. Therefore, Z^* would be equal to t/2nm[168] where t is thickness of the sample. The 2K data of $\Delta\sigma$ (e^2/h) shows a small phase coherence length, L_ϕ, of about 29.98nm indicating the weak WAL effect (figure 3.1d). The results are in accordance with previous WAL data in these family of compounds[169]. The calculated α value -0.449 confirms the WAL effect in the system. This quantum interference effect is significator of metallic state in the strong SOC system. This also indicates an enhanced spin scattering at this temperature. In addition to that, a negative α value confirms the WAL effect at low T and B range. At higher temperature WAL suppressed due to enhanced spin dependent scattering. The fitted values of L_Φ are 29.98nm (A= $-0.14\Omega^{-1}$), 14.21nm (A= $-0.82\Omega^{-1}$), 10.28nm (A= $-1.96\ \Omega^{-1}$) and 5.38nm (A= $-6.73\Omega^{-1}$) at 2, 5, 10 and 25K respectively. Most interestingly, we have found negative magnetoresistance near room-temperature at high field. In a topological system few possibilities are there behind negative MR like- a) chiral anomaly in Weyl semimetals, b) current jetting effects, c) weak localization effect, d) ferromagnetism in the sample and e) field induced magnetic impurity scattering.

The calculated value of α is compared with other reports on TMDs materials in table 3.1.

Table 3.1 The values of α extracted from HLN fitting

Temperature	α	Temperature (K)
$MoTe_2$[170]	-0.41 to -0.51	<2.5
$MoTe_2$[171]	-0.8	1.5
WTe_2[172]	<<1	2
$MoSe_2$[173]	0.56, 0.49	-
MoTeP (**Present work**)	-0.449	2

Observation of the chiral-anomaly induced negative MR requires the applied magnetic field to be parallel to the electric field [152], [174]–[176], which is not our case. An inhomogeneous distribution of the current flowing inside the sample can give rise to negative MR effect and current jetting[177] shows strong dependence on sample geometry/size. However, in our case observed MR is systematically decreased to a negative value and is not observed in the whole range. Furthermore, this effect requires strong preference of the current to flow in the direction of the magnetic field [178]. This also rules out the possibility of current jetting effect in the present investigation. On the other hand, weak localization effects[179], [180] can cause negative magnetoresistance in impurity induced semimetals and semiconductors at low field. When two electron waves interfere constructively while travelling from opposite direction along a closed path, they scatter off by the impurity and leads to an increase in magneto conductivity. In our case, the magnetoconductivity decreases with increase in field, below 1 T indicating the effect of WAL. But at higher field at 300K the observed negative MR cannot be due to the WAL.

It signifies that the magnetism plays an important role in the transition between positive and negative MR for 1T′ MoTeP. The low-field positive MR becomes parabolic like at 300K. Under the application of external magnetic field electronic scattering rate from local moments and impurities is suppressed resulting in increase in transport lifetime that results in a negative magnetoresistance. However, considering such effect for a particular field

range is not appropriate rather we can expect the not so large overall MR effect is due to the ferromagnetism in the sample[178]. Therefore, ferromagnetic ordering throughout the whole temperature range of measurement is the origin of low MR in the system. In fact, ferromagnetic ordering suppresses the scattering which in effect decreases the MR. Moreover, in Weyl semimetal the XMR decreases with increase of temperature and in the present case at 300K the ferromagnetic ordering dominates over the scattering effect leading the negative MR.

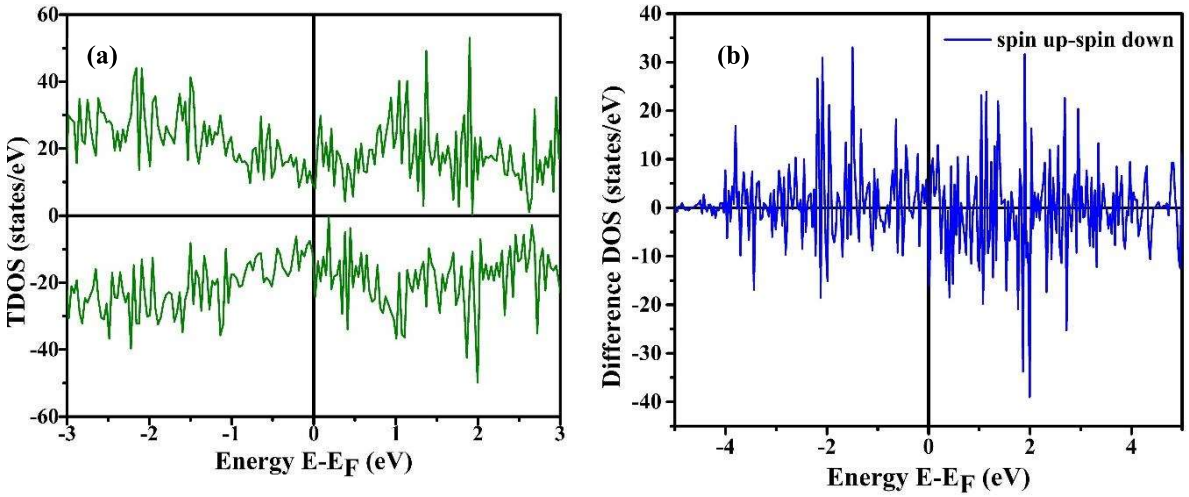

Figure 3.4. (a) Bulk band structure of T_d-MoTeP with inclusion of SOC, **(b)** Spin-resolved Total DOS for defect induced MoTeP.

3.3.5 DFT Calculation In order to further determine the origin of FM ordering we have performed the spin polarized DOS calculation (figure 3.4a). The spin difference It is observed that MoTeP exhibits semimetallic features in bandstructure (Figure 3.5a) similar to parent $MoTe_2$[181]. We speculate that the inclusion of SOC splits the hole and electron bands in two sets of hole and electron pockets with slightly different sizes. The hole bands are comparatively flatter than the electron bands in MoTeP indicating holes possess greater effective mass and smaller mobility than the electrons. This corroborates well with our experimental results. The TOTAL DOS and difference DOS between spin up and spin

down contribution are illustrated in Figure 3.4a and b. The asymmetric total DOS near the Fermi level associated with ferromagnetic behavior of the material. Furthermore, it is observed that Mo-*d* states, Te-*p* and P-*p* have the dominant contribution in their fat band calculations as shown in S5-S7 of supplementary. The total magnetic moment calculated is 2.414 μ_B with defect structure. Without producing defect, the moment is 0.0001 μ_B only. The defect produced moment is close to the magnetic moment calculated for other MoX_2 compounds[127]. Interestingly, incorporation of defects in the crystal structure leads to ferromagnetic interaction from TDOS calculation which is consistent with those already reported[126], [127], [130]. The magnetism mainly promoted by Mo-*4d* orbital states.

We have shown d-band contribution of Mo in the bandstructure in figure 3.5b-e. The contribution of Te-p and P-p states are represented in figure 3.6 a-c and 3.7a-c. The contribution of Mo-d orbital is larger than Te-p and P-p states. The finite DOS at the Fermi level explains the presence of ferromagnetism in the material.

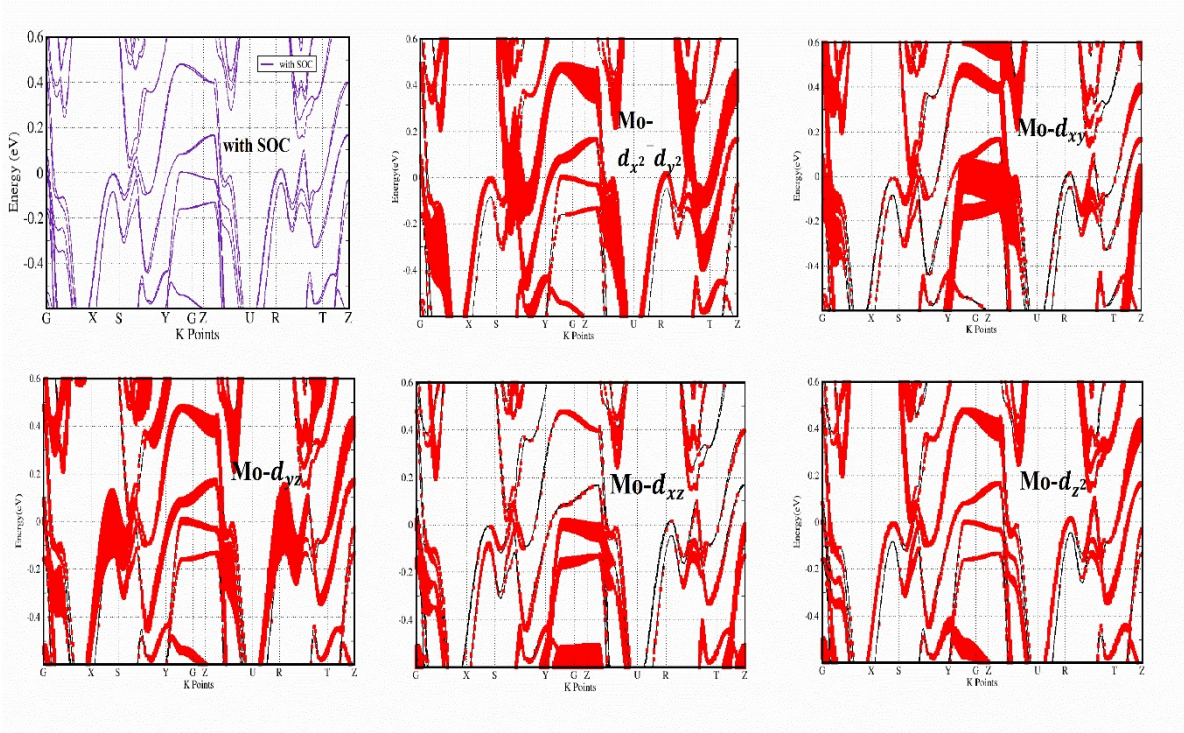

Figure 3.5 (a) Mo-d band contribution in bandstructure.

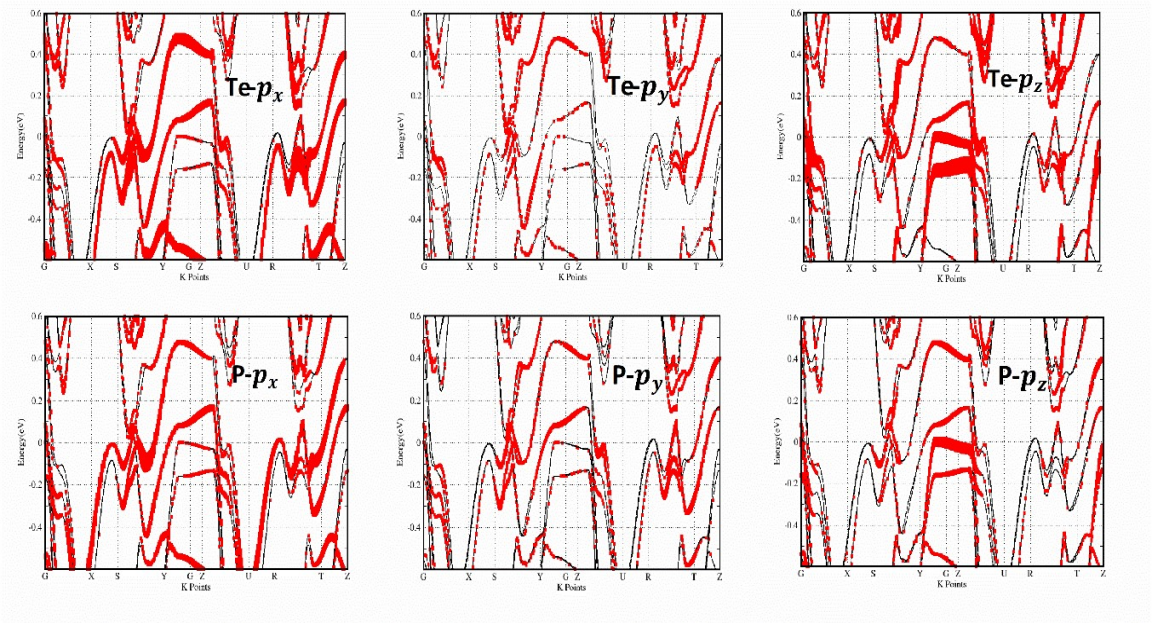

Figure 3.6 (a)-(c) Te-p band contribution in bandstructure, (d)-(f) P-p band contribution in bandstructure.

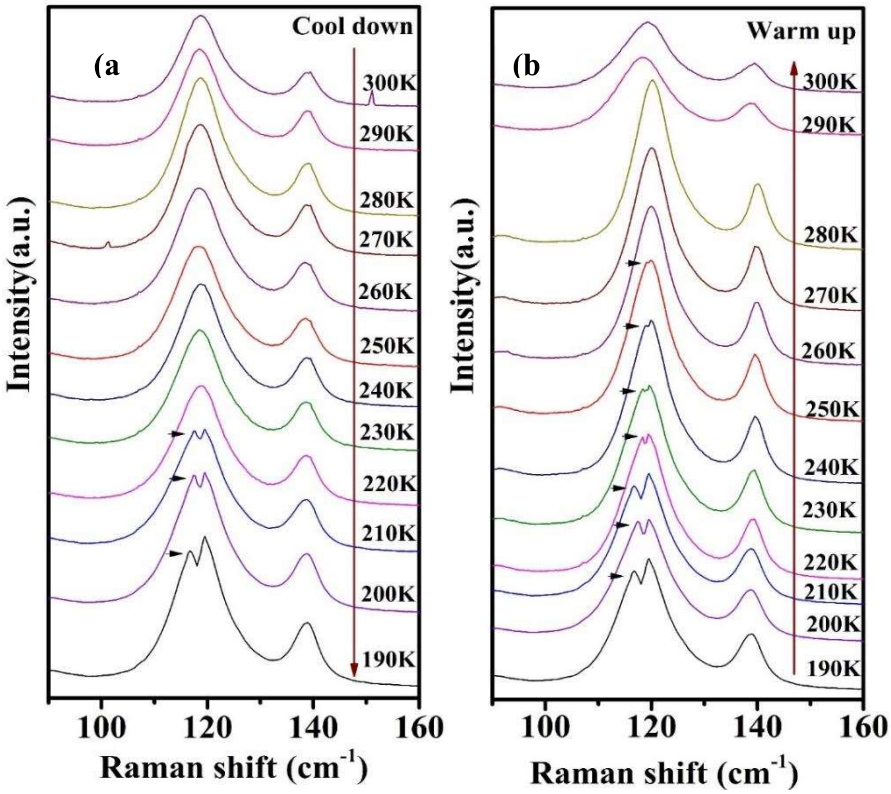

Figure 3.7 Temperature dependent Raman spectra during (a) cooing and (b) heating cycle. The newly obtained mode is noted by arrow at 117.63 cm^{-1} indicating the presence of T_d phase.

3.3.6 Temperature dependent Raman measurements We carried out Raman measurements to explore the origin of thermal hysteresis in both the heating and cooling path as depicted in figure 3.7a and 3.7b. We observed a single mode near 118.59 cm^{-1} to transform into two modes when sample was cooled down to ~220 K. A newly Raman mode at 117.63 cm^{-1} has been inspected as a signature of MoTeP-T_d phase. When the material is heated up to 250K the newly mode completely disappears. This signifies the reappearance of 1T′ phase of MoTeP. The intensity behavior (Figure 3.8a) in the two routes are similar to $MoTe_2$ [140]. This is again indication of the existence of hysteresis in the material.

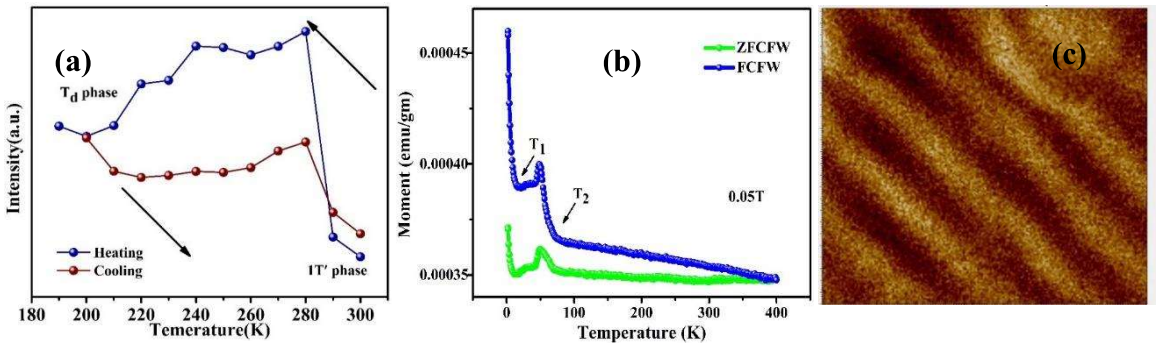

Figure 3.8 (a) Magnetic moment as a function of temperature in ZFC and FC cycle; (b) MFM image taken at room temperature with scan areas 5×5 μm^2.

3.4 Conclusions

We presented a systematic study of magnetotransport and magnetic properties of single-crystalline MoTeP. The semiclassical two-band fitting of the Hall and longitudinal conductivity explain near-perfect carrier compensation at low temperature with very high carrier mobilities. It is evident from the Hall resistivity data that the transport properties in MoTeP are dominated by electron-type charge carriers. The suppressed magnetoresistivity is the result of reduced scattering effects due to the defect induced ferromagnetism. Particularly, at room temperature, this scattering is again suppressed due to the applied high magnetic field. At room temperature ρ_{yx} becomes nonlinear at higher field, implying that both type of carriers is activated. Below 25K, the WAL-induced MR is extremely narrow within 1.5 T. Kohler's scaling of MR% ~ $(B/\rho_0)^m$ with m=1.65 together with a power law

of B^n where n = 1.53 supports the dominating electron charge carrier transport. Departure from linearity above 50K interprets the temperature dependent variation of electron and hole charge carriers. Finally, at room temperature electron and hole joint transport is observed from nonlinear S-shaped Hall data. Importantly, ferromagnetic nature from the asymmetric spin polarized total DOS near Fermi level supports our experimental observation of defect induced ferromagnetic MoTeP. We found incorporation of dopants into the system explored many intriguing features and open up another avenue for future material science research.